Supporting Information

Assembly-Induced Bright Light Emission from Solution-Processed Platinum(II) Inorganic Polymers

Aleksandr Perevedentsev,*[,†,‡] Fabio L. Bargardi,*[,‡] Antoni Sánchez-Ferrer,[#] Nathan J. Cheetham,[⊥] Ahmad Sousaraei,[§] Stephan Busato,[‡] Johannes Gierschner,[§] Begoña Milián-Medina,[△] Raffaele Mezzenga,[#,‡] Reinhold Wannemacher,[§] Juan Cabanillas-Gonzalez,[§] Mariano Campoy-Quiles,[†] Walter R. Caseri[‡]

[†] Institute of Materials Science of Barcelona (ICMAB-CSIC), UAB Campus, Bellaterra, 08193, Spain.
[‡] Department of Materials, ETH Zürich, Vladimir-Prelog-Weg 5, Zürich, 8093, Switzerland.
[#] Department of Health Sciences and Technology, ETH Zürich, Schmelzbergstrasse 9, Zürich, 8092, Switzerland.
[⊥] Department of Physics and Centre for Plastic Electronics, Imperial College London, London SW7 2AZ, United Kingdom.
[§] Madrid Institute for Advanced Studies (IMDEA-Nanociencia), c/ Faraday 9, Ciudad Universitaria de Cantoblanco, Madrid, 28049, Spain.
[△] Department for Physical Chemistry, Faculty of Chemistry, University of Valencia, Avenida Dr. Moliner 50, Burjassot-Valencia, 46100, Spain.

* Corresponding author (A.P. aperevedentsev@icmab.es; F.L.B. fabio.bargardi@mat.ethz.ch).

A.P. and F.L.B. contributed equally to this work.

Table of contents:

1. Materials

The solvents used throughout the study were obtained from:

- N,N-Dimethylformamide (DMF): puriss. p.a., ACS reagent, ≥99.8%, Sigma-Aldrich;
- Chloroform: ≥99.8%, 0.5–1% of ethanol as stabiliser, Sigma-Aldrich;
- Ethanol: puriss. p.a., ACS reagent, ≥99.8%, without additives, Fluka;
- Toluene: puriss. p.a., ACS reagent, ≥99.7%, Fluka;
- Hexane: puriss. p.a., ACS reagent, ≥99%, Sigma-Aldrich;
- Decahydronaphthalene (decalin): mixture of *cis* and *trans* isomers, reagent grade, 98%, Sigma-Aldrich.

All solvents were used as received without further purification.

2. Synthesis and elemental analysis

2.1 Tetrakis(2-ethylhexyl-1-amine)platinum(II) tetracyanoplatinate(II) ('eh-CN')

A solution containing 1100 mg (2.65 mmol) of $K_2[PtCl_4]$ in 20 mL of deionised water was heated to 60 °C under stirring. 2.74 mL (21.2 mmol) of 2-ethylhexyl-1-amine were added to the solution and the mixture was kept stirring at 60 °C. After 5 min the initially red-coloured solution turned yellow and after 30 min a yellow organic phase and a clear aqueous phase were formed. The two-phase solution was cooled to room temperature after 60 min. A second solution containing 1000 mg (2.65 mmol) of $K_2[Pt(CN)_4]$ in 10 mL of deionised water was added to the first solution under stirring. A white precipitate formed immediately and began attaching to the walls of the round-bottomed flask, forming a white ball under movement of the magnetic stirrer. The aqueous part of the solution was decanted and the flask dried in vacuum for 2 h. The product was then redispersed in 15 mL of chloroform at 60 °C under stirring followed by cooling to room temperature. Adding 40 mL of ethanol yielded a translucent white dispersion. The product was filtered through a sintered glass funnel (P4, 7.5 µm pore diameter), rinsed sequentially with 5 mL of water and ethanol, and finally dried at 10^{-2} mbar. Yield: 1975 mg, 74%.

2.2 Tetrakis(4-phenyl-1-butylamine)platinum(II) tetracyanoplatinate(II) ('dmoc-CN')

A solution containing 220 mg (0.53 mmol) of $K_2[PtCl_4]$ in 2 mL of deionised water was heated to 60 °C under stirring. 0.53 mL (3.39 mmol) of 3,7-dimethyloctan-1-amine were added to the solution and the mixture was kept stirring at 60 °C. After 30 min a yellow organic phase and a clear aqueous phase were formed. The two-phase solution was cooled to room temperature after 60 min. A second solution containing 200 mg (0.53 mmol) of $K_2[Pt(CN)_4]$ in 1 mL of deionised water was added to the first solution under stirring. A white precipitate formed after 20 min which then agglomerated into spheres and began attaching to the surface of the flask. The aqueous part of the solution was decanted and the product was washed twice with 3 mL of water to completely remove K^+ and Cl^- ions, after which it was dried in vacuum for 2 h. For

the purpose of purification the product was subsequently redispersed in 2 mL of chloroform at room temperature under stirring, precipitated by the addition of 10 mL of ethanol and filtered through a sintered glass funnel (P4, 7.5 µm pore diameter) over a period of 2 h. Finally the product was rinsed with 2 mL of ethanol and dried at 10^{-2} mbar. Yield: 431 mg, 72%.

2.3 Elemental analysis

Table S1. Summary of elemental analysis for the synthesised TCN-MS derivatives, $[Pt(NH_2R)_4][Pt(CN)_4]$ where *R* is a solubilising group (branched alkyl or ω-phenylalkyl), showing the values obtained for chemical composition as well as the corresponding theoretically calculated values. All values are given in wt% units. See Fig. 1 in the main text for an explanation of the nomenclature adopted for the naming of the compounds.

Compound		C	H	N	Pt
mh-CN	*found*	42.64%	7.46%	11.17%	
	calc.	42.76%	7.58%	11.08%	38.58%
pb-CN	*found*	48.46%	5.79%	10.15%	
	calc.	48.43%	5.54%	10.27%	35.76%
dmoc-CN	*found*	47.00%	8.34%	9.98%	
	calc.	47.04%	8.25%	9.97%	34.73%
eh-CN	*found*	42.83%	7.83%	11.31%	
	calc.	42.76%	7.58%	11.08%	38.58%

3. Characterisation of dissolved TCN-MS derivatives

3.1 IR spectroscopy

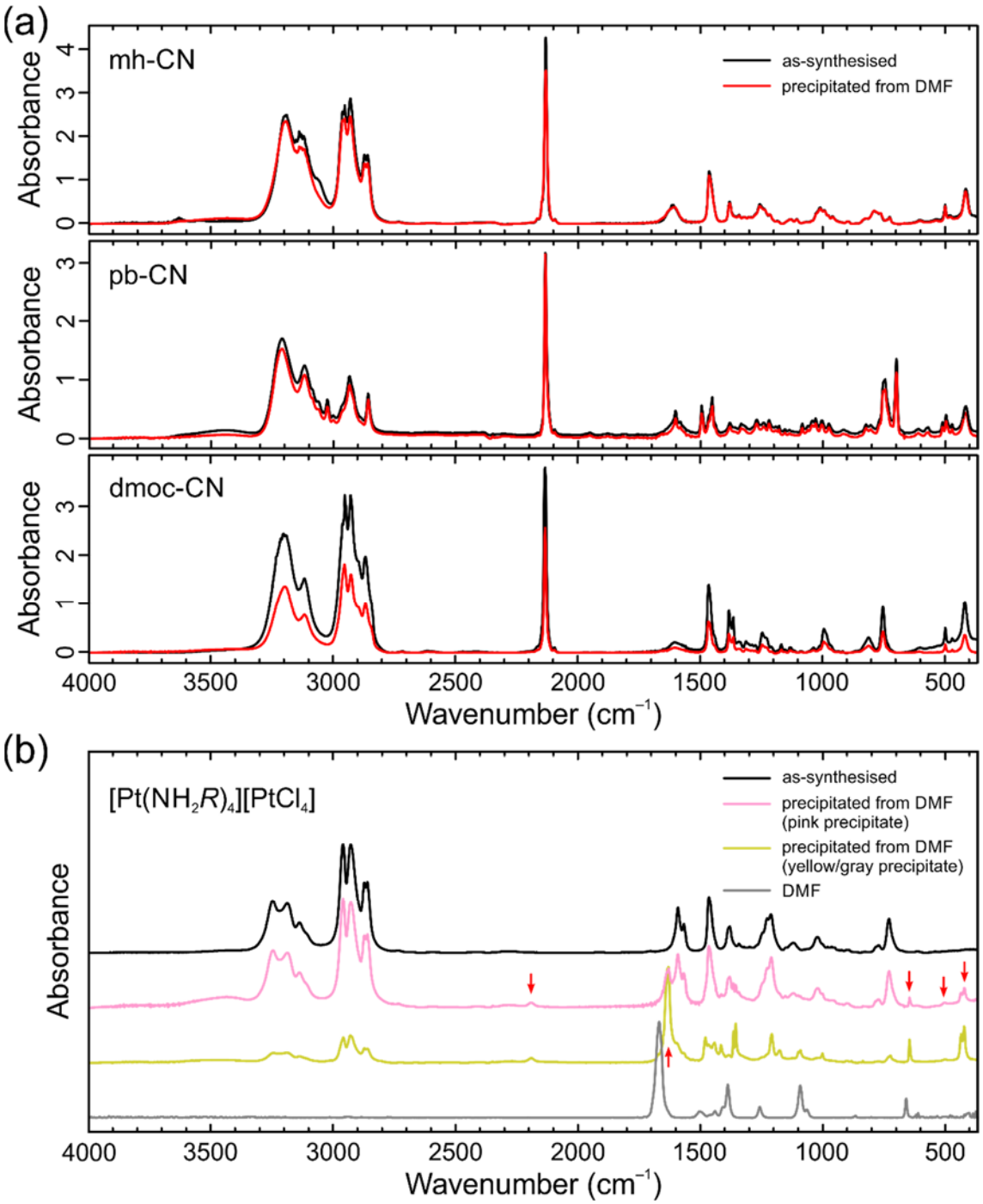

Figure S1. (a) IR spectra of TCN-MS compounds: as-synthesised (*black lines*) and following dissolution in DMF and re-precipitation by evaporation of solvent (*red lines*). **(b)** IR spectra of $[Pt(NH_2R)_4][PtCl_4]$ where *R* = 6-methyl-1-heptyl ('mh') – the tetrachloroplatinate analogue of mh-CN – as-synthesised (black line) and following dissolution in DMF and re-precipitation by evaporation of solvent (*pink and yellow lines*). Red arrows highlight the new peaks that emerge for the DMF-treated compound. The spectrum of neat DMF (*grey line*) is also shown.

Table S2. Summary of elemental analysis for TCN-MS derivatives following dissolution in DMF and reprecipitation f by evaporation of solvent, showing the values (in wt% units) obtained for chemical composition as well as the corresponding theoretically calculated values. Note that the match is as good as, or better, as for the pristine, as-synthesised compounds (compare with Table S1 above), indicating a purifying effect of dissolution in DMF. Also shown are the corresponding values for an alkyl-substituted tetrachloroplatinate MGS derivative, $[Pt(NH_2R)_4][PtCl_4]$ where *R* = 6-methyl-1-heptyl, revealing a significant deviation in chemical composition following dissolution in DMF. See Fig. 1 in the main text for an explanation of the nomenclature adopted for naming of the compounds.

Compound		C	H	N	Cl	Pt
mh-CN	*found*	42.65%	7.65%	11.12%	—	
	calc.	42.76%	7.58%	11.08%	—	38.58%
pb-CN	*found*	48.16%	5.68%	10.29%	—	
	calc.	48.43%	5.54%	10.27%	—	35.76%
dmoc-CN	*found*	46.98%	8.36%	9.93%	—	
	calc.	47.04%	8.25%	9.97%	—	34.73%
$[Pt(NH_2mh)_4][PtCl_4]$	*found*	33.64%	6.56%	5.24%	13.18%	
	calc.	36.64%	7.30%	5.34%	13.52%	37.20%

3.2 Small-angle X-ray scattering

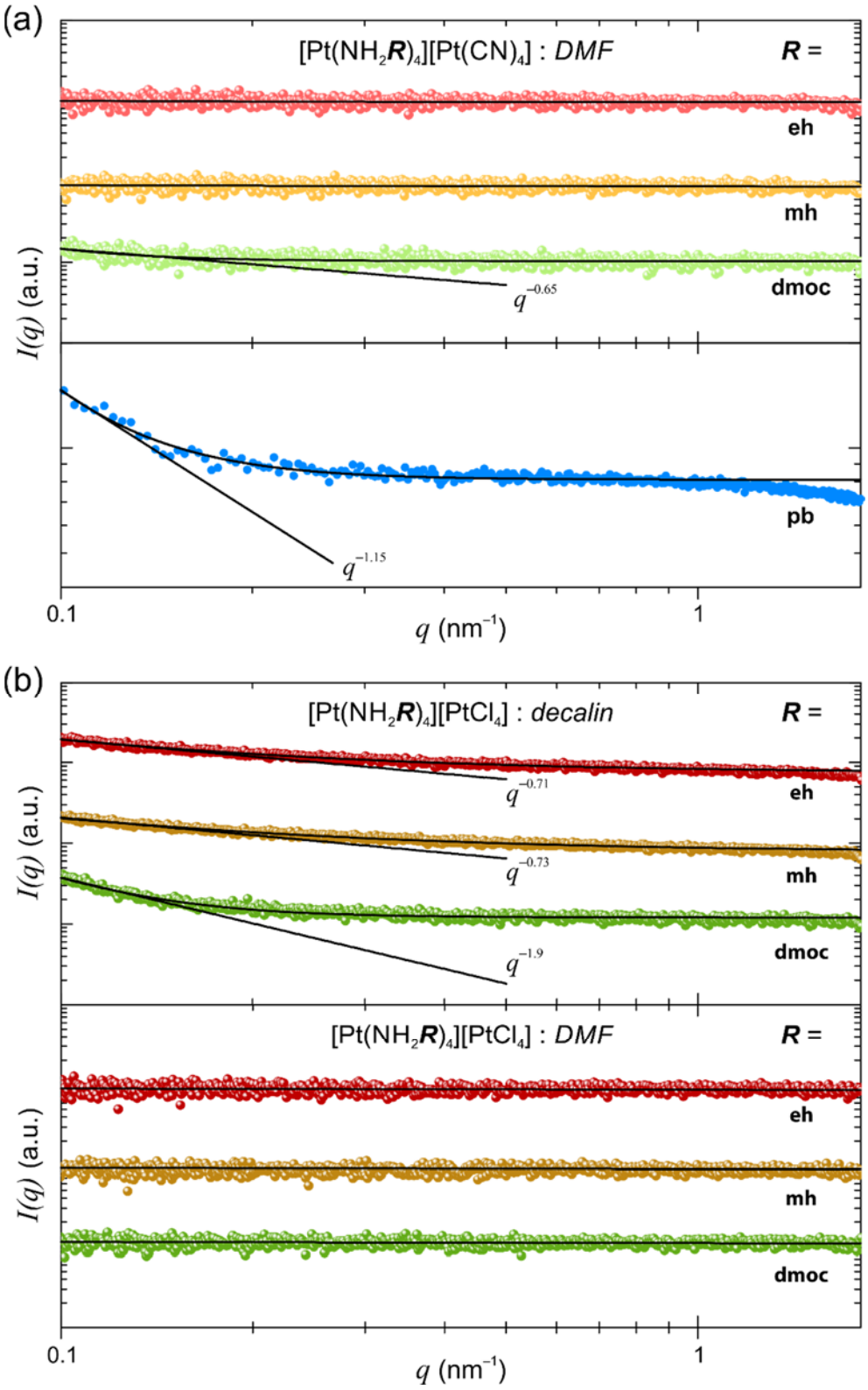

Figure S2. Small-angle X-ray scattering (SAXS) patterns for **(a)** TCN-MS derivatives reported in this work and **(b)** alkyl-substituted Magnus' green salt derivatives, $[Pt(NH_2R)_4][PtCl_4]$ where *R* is the indicated alkyl group, in solutions with DMF or decalin. The slopes are indicated.

4. Optical microscopy of films of unassembled and assembled dmoc-CN

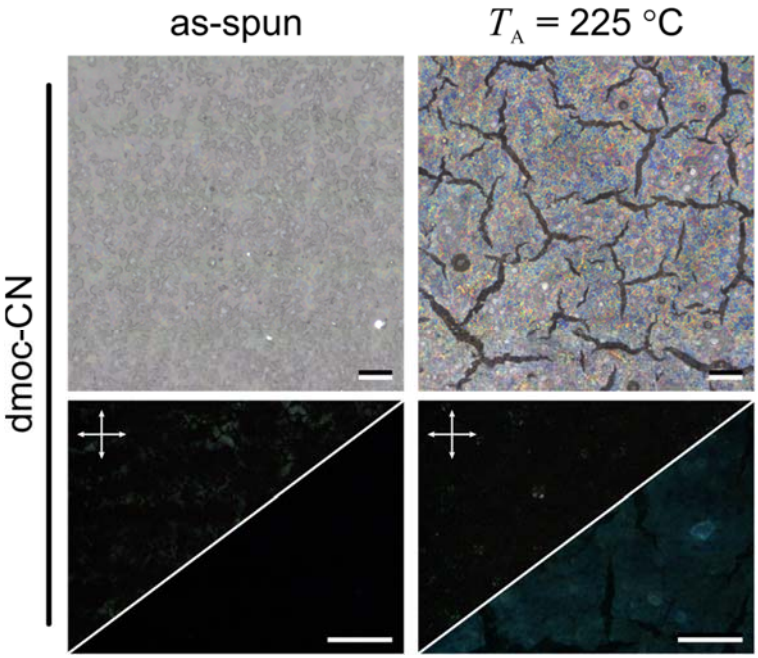

Figure S3. Optical micrographs of dmoc-CN films recorded following assembly at selected temperatures, T_A, and etching of PEO. *Left*: as-spun; *right*: T_A = 225 °C. *Top panels*: reflected-light micrographs; *bottom panels*: cross-polarised transmitted light and fluorescence micrographs (top-left and bottom-right, respectively). Scale bar = 25 μm. Note the extremely weak photoluminescence for assembled dmoc-CN (*bottom-right*).

5. Topography of assembled films: crack formation and phase-separation-induced surface features

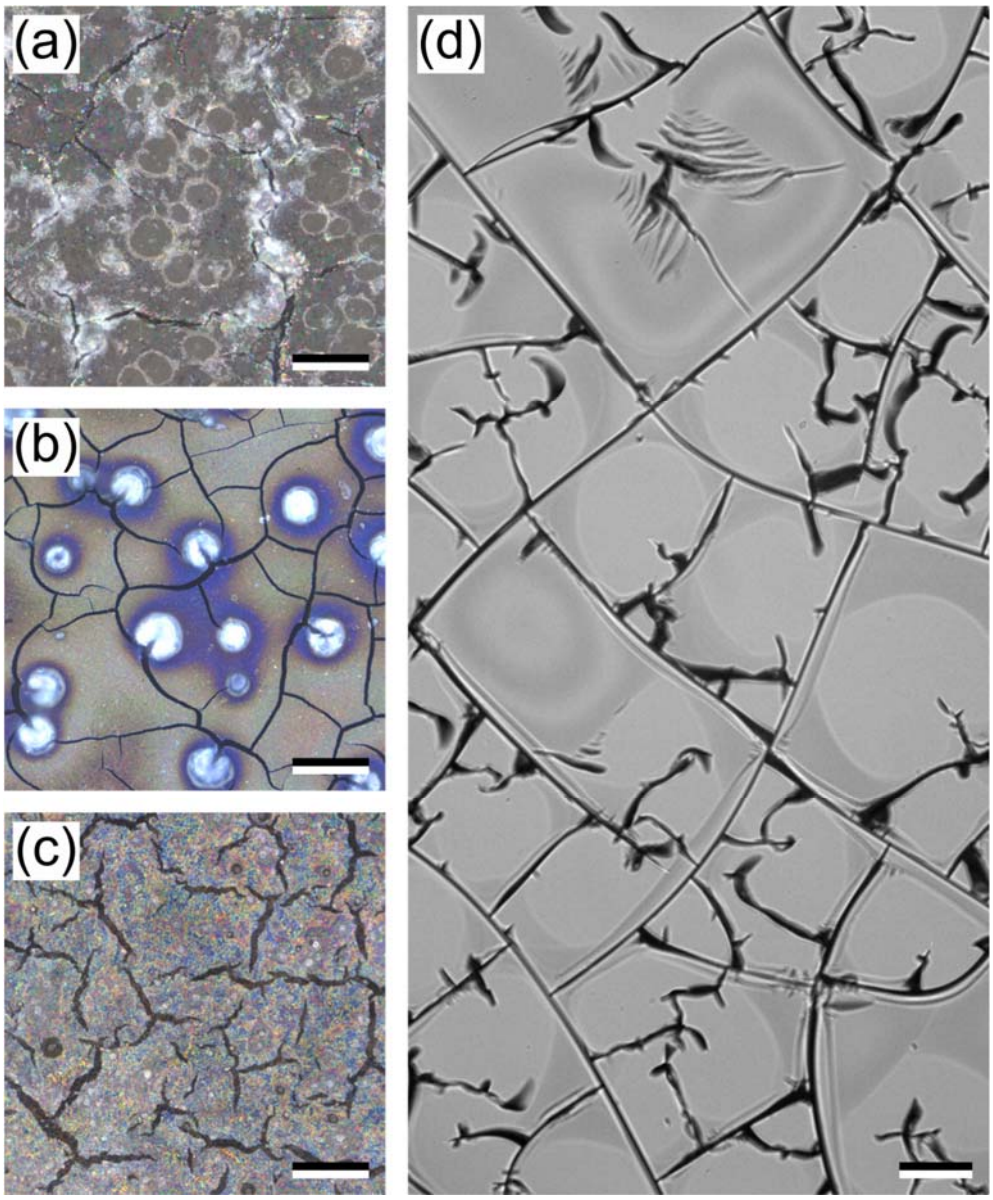

Figure S4. Reflected-light micrographs of **(a)** mh-CN, **(b)** pb-CN and **(c)** dmoc-CN films recorded following assembly at T_A = 225 °C and etching of PEO. For reference, **(d)** shows a film of poly(2,4,6-trimethyl phenylenemethylene) (P3MPM; see Braendle et al., *J. Polym. Sci., Part B: Polym. Phys.* **2017**, *55*, 707) that was swelled by immersion in acetone, followed by rapid solvent evaporation. The resulting mechanical stress caused the formation of cracks in the brittle (T_g = 147 °C) film of the relatively low molar mass (M_n = 5000 g mol^{-1}) polymer. Scale bar = 50 μm.

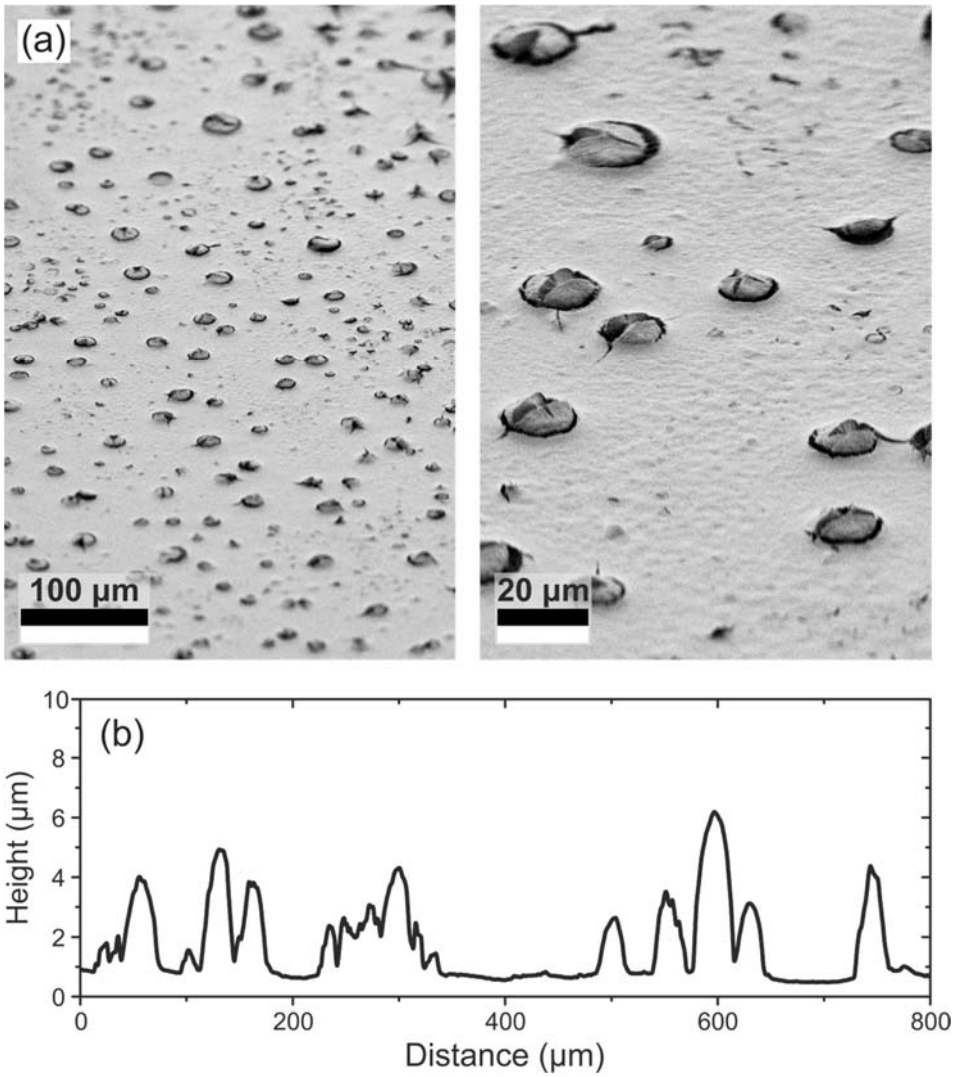

Figure S5. Analysis of topography of a assembled pb-CN film (T_A = 225 °C). **(a)** Scanning electron microscopy (SEM) micrographs, recorded at *glancing incidence* (i.e. samples tilted with respect to the incident electron beam). 'Goose-skin' texture resulting from phase-separation during assembly is evident. SEM was performed with a LEO 1530 Gemini instrument using secondary electron detection. (*N.B.* Since these micrographs were acquired at the extreme edge of the film, the characteristic crack pattern is not seen – most likely due to higher film thickness at substrate edges.) **(b)** Topography profile of the film measured by surface profilometry. The dimensions of the raised areas match those of the hemispherical aggregates observed by SEM and optical microscopy.

6. Confocal PL microscopy of TCN-MS films at different degrees of assembly

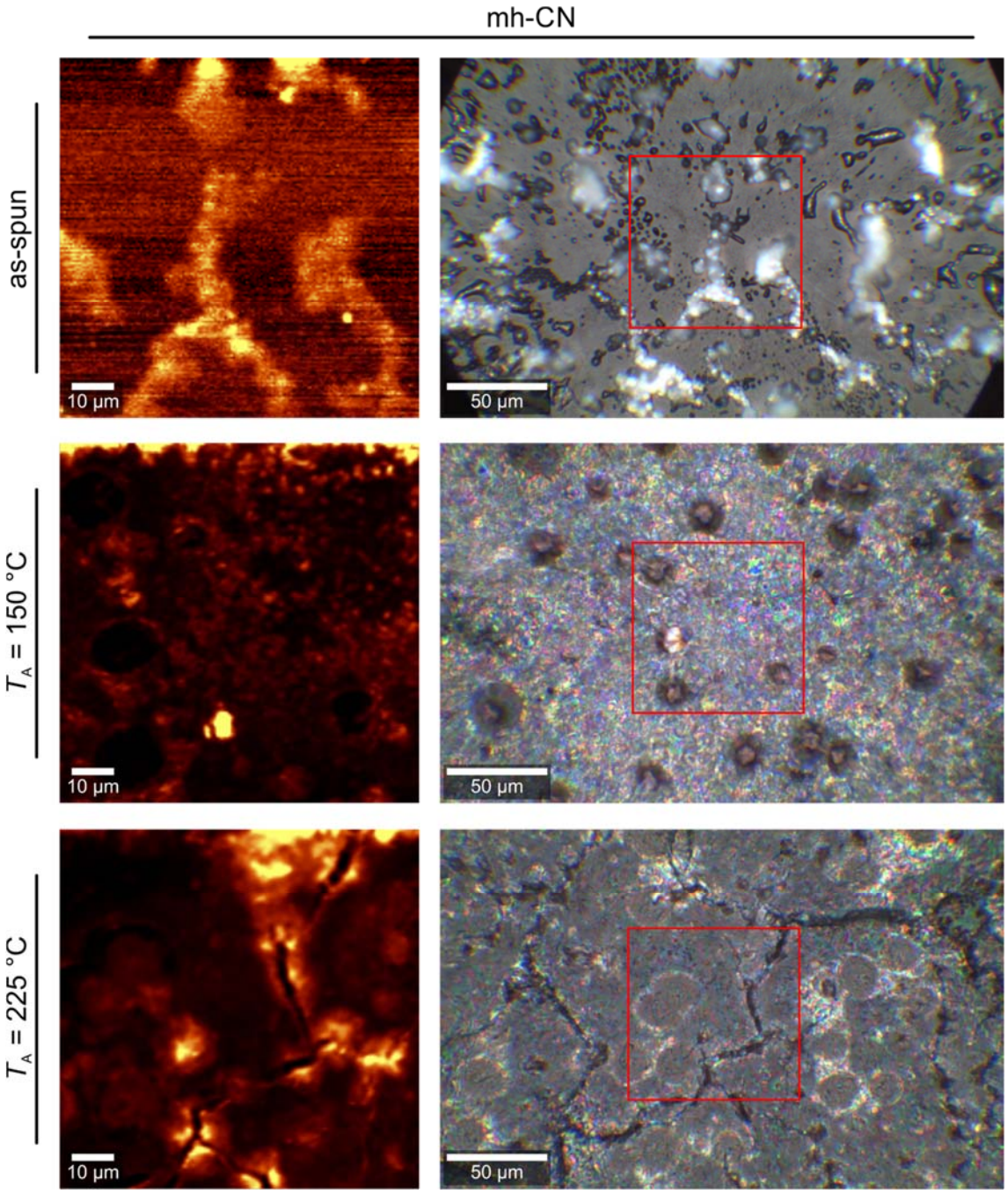

Figure S6. Optical and confocal PL micrographs of mh-CN films recorded following assembly at the indicated temperatures and removal of PEO. *Left*: confocal PL images recorded with excitation at 355 nm and detection at 500–520 nm. *Right*: reflected-light microscopy; red squares highlight the areas for which the confocal PL images were acquired.

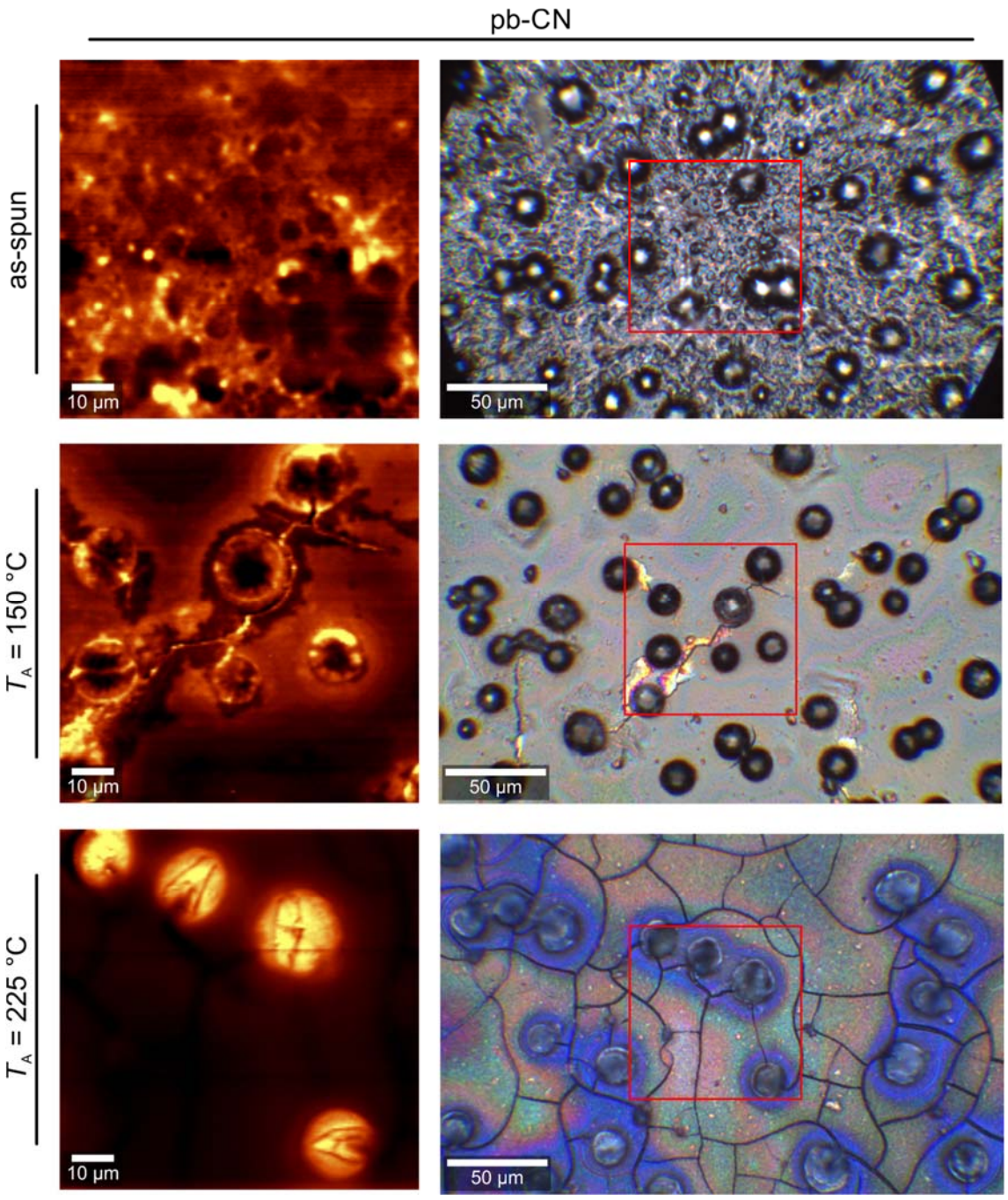

Figure S7. Optical and confocal PL micrographs of pb-CN films recorded following assembly at the indicated temperatures and removal of PEO. *Left*: confocal PL images recorded with excitation at 355 nm and detection at 500–520 nm. *Right*: reflected-light microscopy; red squares highlight the areas for which the confocal PL images were acquired.

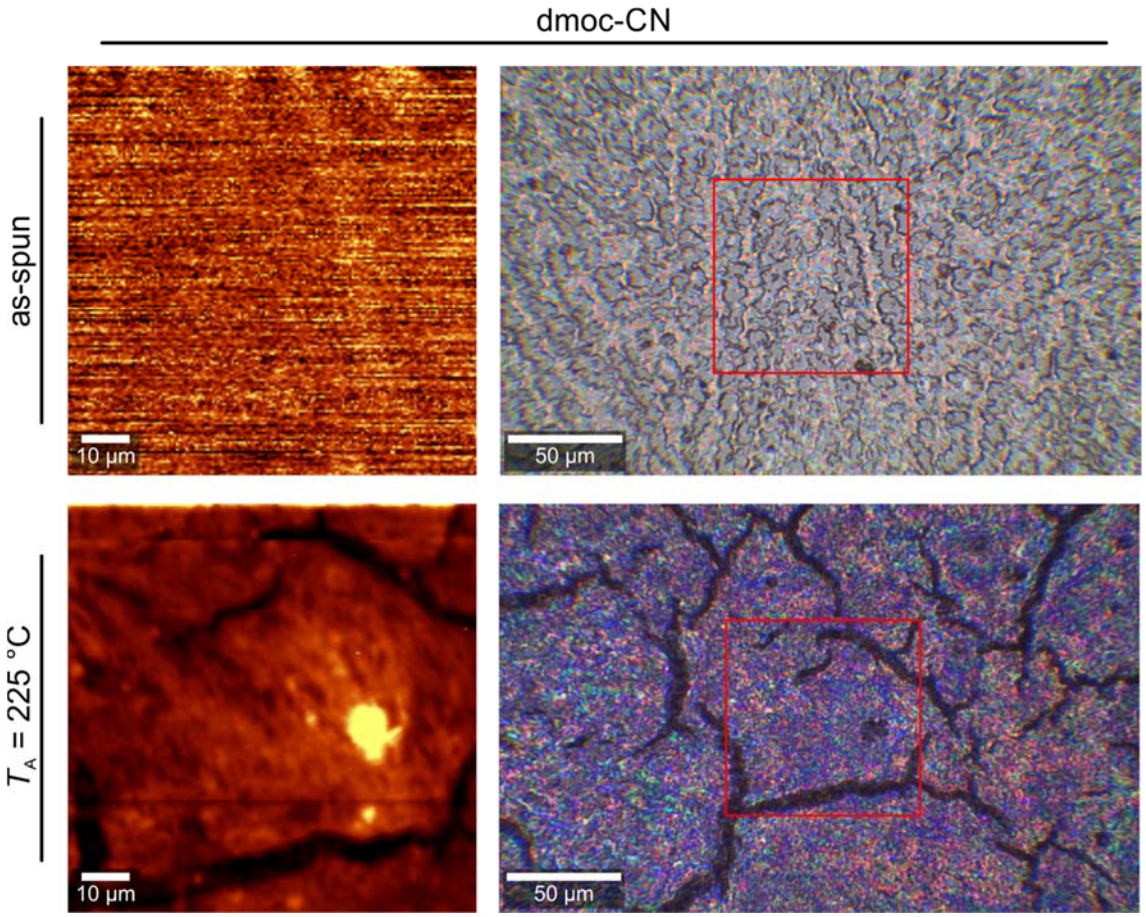

Figure S8. Optical and confocal PL micrographs of dmoc-CN films recorded following assembly at the indicated temperatures and removal of PEO. *Left*: confocal PL images recorded with excitation at 355 nm and detection at 500–520 nm. *Right*: reflected-light microscopy; red squares highlight the areas for which the confocal PL images were acquired.

Note that the colour scale (absolute counts) is *relative* in all cases (Figs. S6–S8). In fact, for the films of assembled dmoc-CN (Fig. S8, bottom row) the average intensity (counts) is ×5 lower than that for, for instance, assembled mh-CN (Fig. S6, bottom row). This is readily confirmed by a comparison of fluorescence microscopy images in Fig. 2 in the main text and Fig. S3 herein.

7. Raman spectroscopy

Table S3. Assignment of selected vibrational modes observed in the Raman spectra recorded for TCN-MS derivatives in solution-processed thin films (as-spun and assembled at T_A = 150 and 225 °C, with subsequent etching of PEO).

Raman shift (cm^{-1})	Compounds	Assignment
315	*all – assembled*	ν(Pt–CN)
356	*all – assembled*	δ(Pt–CN)
403	*all – assembled*	γ(Pt–CN)
506	*all – assembled*	ν(Pt–C)
621	pb-CN	in-plane distortion of phenyl ring
748	pb-CN	breathing of phenyl ring
827–834	*all*	ν(C–C)
1002	pb-CN	breathing of phenyl ring
1031	pb-CN	ν(C–C), δ(C–H) (phenyl ring)
1156	pb-CN	δ(CH)
1296	*all*	ϖ(CH2), δ(CH), ρ(CH_2)
1307	*all*	ϖ(CH_2), τ(CH_2)
1453	*all*	δ(CH_3) asym., δ(CH_2)
1583, 1604	pb-CN	degenerate ν(C–C) (phenyl ring)
2146, 2203	*all – as-spun*	
2148–2151, 2214–2219	*all – T_A = 150 °C*	ν(C≡N)
2151, 2224, 2244	*all – T_A = 225 °C*	

Abbreviations: γ = out-of-plane bending, δ = in-plane bending, ν = stretching, ρ = rocking, τ = twisting, ϖ = wagging.

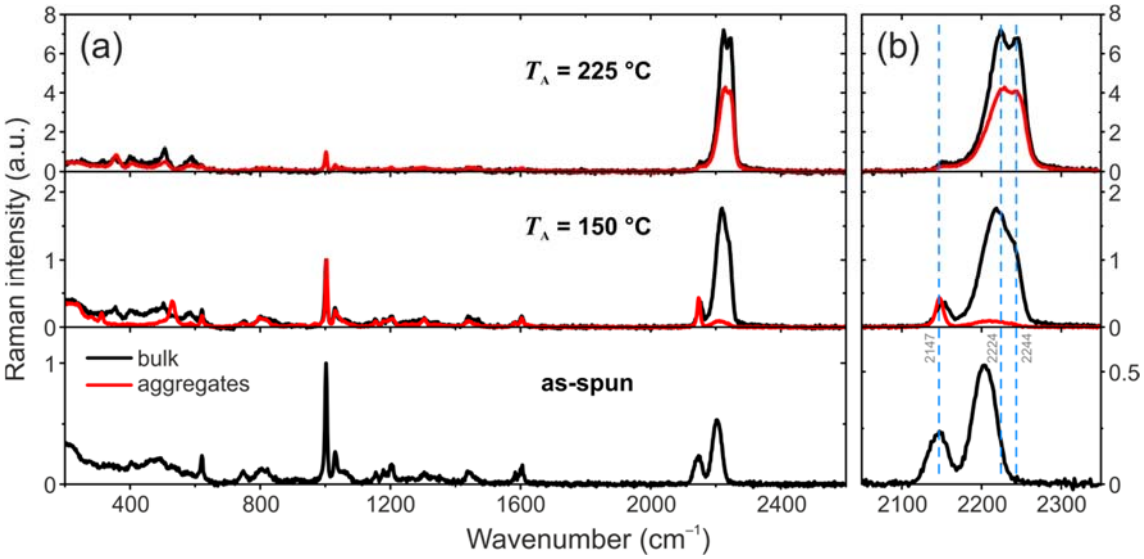

Figure S9. Raman spectra for pb-CN films recorded following assembly at the indicated temperatures, T_A, and etching of PEO. Spectra were acquired at the bulk/non-aggregated locations (*black lines*) and the centres of aggregates (*red lines*). All data are normalised by the maximum intensity of the 1002 cm^{-1} (phenyl ring breathing) mode. **(a)** shows the full spectra; an expanded view of the spectral region corresponding to υ(C≡N) vibrations is shown in **(b)**. The spectral positions of selected peaks are indicated.

8. Intra-chain structure and bonding

Table S4. Bond lengths (Å) and angles (°) for $[Pt(NH_2\mathbf{CH_3})_4][Pt(CN)_4]_n$ optimised by DFT.

	n = 8	**n = 1**
$d(Pt–Pt_{out})$	3.27	3.30
$d(Pt–Pt_{in})$	3.20	—
d(Pt–C)	2.00	2.00
d(C≡N)	1.16	1.16
d(Pt–N)	2.11	2.10
$d(N–C_{NH2R})$	1.48	1.48
$d(N_{CN}\cdots H_{NH2R})$	2.39	2.02
α(Pt–C≡N)	177°	166°
β(Pt–N–C)	122°	122°
θ(N–Pt–Pt–C)	24°	26°
$\phi(N–Pt–N–CH_3)$	1°	6°

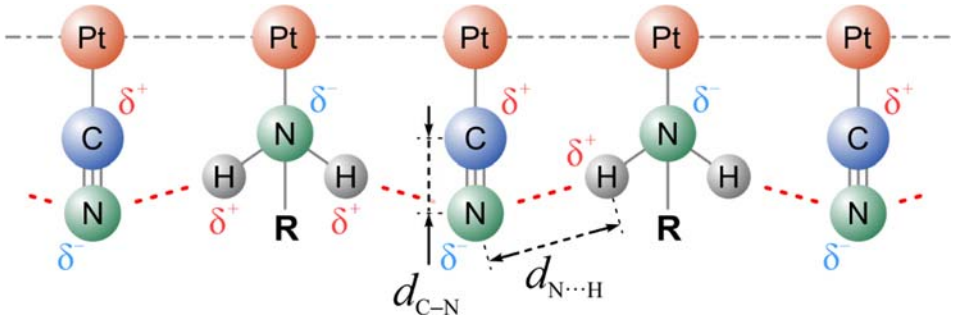

Figure S10. Schematic 2D illustration of the proposed intra-chain electrostatic bonding between partially-positive H atoms of NH_2R groups and partially-negative N atoms of cyanide groups on adjacent ions. Interatomic C–N and N···H distances d are indicated by the arrows.

Table S5. Assignment of selected vibrational modes observed in the IR spectra for TCN-MS derivatives (as-spun and assembled at T_A = 150 and 225 °C, with subsequent etching of PEO).

Wavenumber (cm^{-1})	**Compounds**	**Assignment**
1379, 1464	*all*	$\delta(CH_2)$
1600	*all except fully assembled*	$\delta(NH_2)$
2123–2216	*all*	ν(–C≡N)
2857–2980	*all*	ν(C–H)
3134, 3217	*all except fully assembled*	ν(N–H)

Abbreviations: δ = in-plane bending, ν = stretching.

9. Nucleation of TCN-MS derivatives using DMDBS

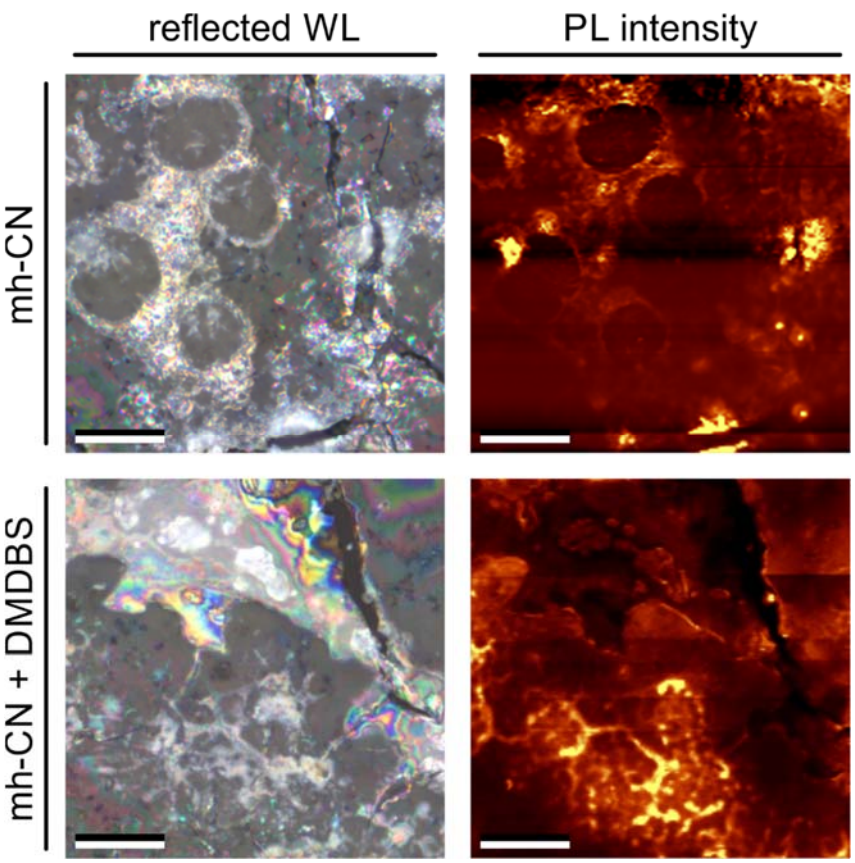

Figure S11. Optical and confocal PL micrographs of mh-CN films recorded following assembly at T_A = 225 °C and etching of PEO (as in Fig. 8(a)). Films were processed from solutions without DMDBS (*top panels*) and with 2 wt% DMDBS added relative to mh-CN loading (*bottom panels*). *Left panels*: reflected-light micrographs; *right panels*: integrated PL intensities recorded for the same sample areas (λ_{ex} = 488 nm). Scale bar = 20 μm. Note the disappearance of weakly-luminescent dark spots (*top-right*) in the neat mh-CN film upon nucleation by DMDBS (*bottom-right*).

10. Time-resolved photoluminescence spectroscopy

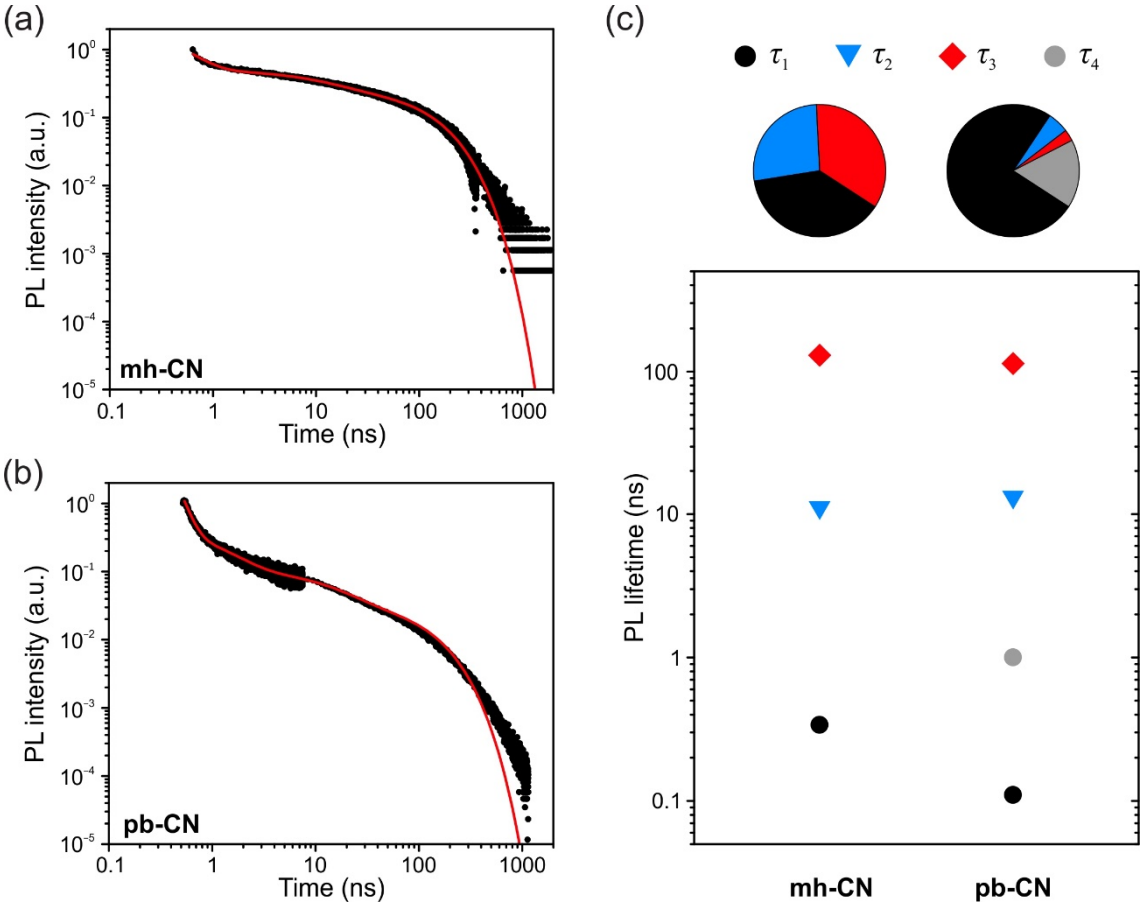

Figure S12. PL decays for assembled **(a)** mh-CN and **(b)** pb-CN recorded with detection at 534 and 521 nm respectively. Both data (•) and fits (*red lines*) are shown. **(c)** Summarised fitting results for the PL lifetime data in (a,b) showing the lifetimes of the constituent exponential decay components (*lower panel*) as well as their relative amplitudes (*upper panel*).

Table S6. Fitting results for time-resolved PL spectroscopy data showing, in each case, the relative amplitudes and lifetimes of the exponential decay components, as well as the amplitude-weighted average lifetime τ_{av}.

Material	χ^2	A_1 (%)	τ_1 (ns)	A_2 (%)	τ_2 (ns)	A_3 (%)	τ_3 (ns)	A_4 (%)	τ_4 (ns)	τ_{av} (ns)
mh-CN	0.996	38.3	0.34	26.7	10.99	35.0	129.87	–	–	48.48
pb-CN	0.990	75.2	0.11	5.2	13.00	2.8	114.00	16.7	1.00	4.16

The PL decays (Figure S12) were 'stitched' together by overlapping individual decay traces recorded with excitation at 405 nm (time range below 7.6 ns) and 355 nm (time range below 1 μs). The PL decays were then fitted by a sum of exponential components (Table S6), allowing the amplitude-weighted average PL lifetime, τ_{av}, to be estimated. Note that the deviation seen beyond 500 ns has a negligible effect on τ_{av} owing to the low PL intensity in this range (<10^{-3}

a.u.). We further note that 'stitching' of PL decays recorded with excitation using two different laser sources (355 and 405 nm) introduces a number of uncertainties, namely (i) potential excitation of different species resulting in a different amount of excess energy for the photogenerated excitons and (ii) different fluence which can vary the propensity for, e.g., exciton-exciton annihilation. Nevertheless, the adopted analytical approach was deemed to be favourable overall given that it provides a more complete representation of PL decay kinetics.

It is also interesting to note the difference in the obtained τ_{av} values for assembled mh- and pb-CN (48.5 and 4.2 ns respectively). As shown in in Figure S12(c), the long-lived PL components ($\tau >$ 10 ns) have a much smaller contribution to the overall PL decay of pb-CN than for mh-CN. At present it remains difficult to confirm whether this difference arises from the different purity of the analysed compounds (i.e. the different concentration of quenching sites) or structural features of assembled quasi-1D 'polymeric' stacks. Further analysis, e.g. temperature-dependent PL lifetime measurements, will be needed to elucidate the origin of this difference in photophysical properties.